Physics in Medicine and Biology

Quantifying the ultrastructure of carotid artery using high-resolution micro-diffusion tensor imaging – comparison of intact vs. open cut tissue

To cite this article before publication: Syed Salman Shahid *et al* 2017 *Phys. Med. Biol.* in press https://doi.org/10.1088/1361-6560/aa9159

Quantifying the ultrastructure of carotid artery using high-resolution micro-diffusion tensor imaging – Comparison of intact vs. open cut tissue

***Syed Salman Shahid[1,2,5], Robert Gaul[1,2], Christian Kerskens[3], Vittoria Flamini[4], **Caitríona Lally[1,2]**

[1]Trinity Centre for Bioengineering, Trinity College Dublin, Ireland.

[2]Department of Mechanical and Manufacturing Engineering, School of Engineering, Trinity College Dublin, Ireland.

[3]Trinity College Institute of Neuroscience, Trinity College Dublin, Ireland

[4]Department of Mechanical and Aerospace Engineering, NYU Tandon School of Engineering, Brooklyn, NY, USA

[5]Department of Neurology, Emory University School of Medicine, Atlanta, GA, USA

[*]email: syed.salman.shahid@emory.edu, salman_cae@hotmail.com

****lallyca@tcd.ie**

***ORCID : 0000-0002-0914-6933**

Abstract

Diffusion magnetic resonance imaging (dMRI) can provide insights into the microstructure of intact arterial tissue. The current study employed high magnetic field MRI to obtain ultra-high resolution dMRI at an isotropic voxel resolution of 117 μm^3 in less than 2 hours of scan time. A parameter selective single shell (128 directions) diffusion-encoding scheme based on Stejskel-Tanner sequence with echo-planar imaging (EPI) readout was used. EPI segmentation was used to reduce the echo time (TE) and to minimise the susceptibility-induced artefacts. The study utilised the dMRI analysis with diffusion tensor imaging (DTI) framework to investigate structural heterogeneity in intact arterial tissue and to quantify variations in tissue composition when the tissue is cut open and flattened. For intact arterial samples, the region of interest (ROI) base comparison showed that the differences in fractional anisotropy (FA) and differences in mean diffusivity (MD) across the media layer were significantly higher ($p < 0.05$). For open cut flat samples, DTI based directionally invariant indices did not show significant differences across the media layer. For intact samples, fibre tractography based indices such as calculated helical angle and fibre dispersion showed near circumferential alignment and a high degree of fibre dispersion, respectively. This study demonstrates the feasibility of fast dMRI acquisition with ultra-high spatial and angular resolution at 7T. Using the optimised sequence parameters, this study shows that DTI based markers are sensitive to local structural changes in intact arterial tissue samples and these markers may have clinical relevance in the diagnosis of atherosclerosis and aneurysm.

INTRODUCTION

The health of a blood vessel is highly susceptible to changes in the composition of its underlying microstructural environment. Arterial tissue is composed of vascular smooth muscle cells (VSMC) embedded in an extracellular matrix (EMC), comprising elastin and collagen fibres and glycosaminoglycans (GAGs) [1]. The arrangement of these microstructural elements within the arterial tissue is the major contributing factor in defining its complex mechanical characteristics. Changes in the composition of the arterial microstructural environment occur during the normal course of ageing and also due to pathological adaptation (remodelling) [2, 3]. Age related changes, such as stiffening of arterial walls and arteriosclerosis are associated with an increase in collagen contents [4, 5]. Similarly, hypertension is associated with an increase in the production of elastin and collagen [6]. Blood vessels with such pathologies exhibit stark differences in their tissue microenvironment compared to healthy arteries. Since the arterial microenvironment plays an important role in regulating the vessel health, pathological changes in the blood vessel are often associated with changes in VSMC composition [7] and changes in collagen fibre orientation [8, 9].

There are several (invasive and non-invasive) methods to map the arterial microstructure at multiple scales. Invasive methods usually rely on histological sectioning for cross-comparison. These methods include scanning electron microscopy (SEM) [10, 11], polarised light microscopy (PLM) [12], and second harmonic generation (SHG) [13] to name but a few. Most of these studies have been carried out on fixed vessels which can alter the mechanical composition of the native tissue [14]. Non-destructive methods such as: optical coherence tomography (OCT) and polarisation sensitive optical coherence tomography (PS-OCT) [15, 16], magnetic resonance imaging (T2, T2* - weighted MRI) [12, 17] and diffusion tensor imaging (DTI) [18-21] have also been shown capable of capturing the microstructural profile with limited success. These imaging techniques are crucial for elucidating the biomechanical behaviour of the blood vessels and identifying possible biomarkers associated with specific pathologies. Even though some of these methods can provide sub-micron level details of the arterial ultrastructure, their success as a clinical marker is somewhat limited, as they are generally applied to small excised and fixed sections of the blood vessel.

Of all these methods, diffusion tensor imaging based markers have the potential to estimate structural variations associated with changes in the microenvironment of the arterial tissue in vivo. Such biomarkers would be highly valuable to elucidate the mechanical response of the ultrastructure under certain pathologies. The aim of this paper is to evaluate the sensitivity of DTI-based biomarkers to detect structural variations in intact arterial tissue and to quantify changes in tissue composition when its structural integrity is compromised. To achieve this task, ultra-high spatial and angular resolution dMRI was carried out on intact and open cut (flat) samples. High field MRI can provide better SNR which can be translated into higher spatial resolution, however, at higher fields, the signal from single-shot EPI DWI decays much faster due to shorter T2 and T2* decay times [22, 23]. T2* relaxation is highly sensitive to susceptibility-induced off-resonance field and at higher field strengths the magnetic susceptibility induced inhomogeneity causes a much sharper decay in T2* relaxation profile [22]. Other factors such as poor shimming can also exacerbate the distortion artefacts. To overcome these technical challenges, the proposed study acquired DWI with multi-segmented EPI readout [24]. By dividing the k-space into multiple interleaved acquisitions, the susceptibility induced inhomogeneities were reduced and the T2 relaxation time was also reduced from 90 ms to 26 ms. Using the optimised DWI acquisition protocol, the proposed study employs DTI framework on ultra-high resolution (isotropic) DWIs to quantify heterogeneity in the microenvironment of intact arterial tissue in a fast and robust manner. The study demonstrates the suitability of DTI-based indices as potential biomarkers to distinguish region-wise variations in intact

arterial tissue. The study also demonstrates the role of residual stresses in maintaining the heterogeneity in the arterial microenvironment.

MATERIALS AND METHODS

Sample preparation

Nine samples of fresh porcine common carotid arteries were harvested from Large White pigs aged 6 months with an approximate weight of 80 kg each. The samples were transported on ice and processed within 2 hours of slaughter. The harvested arteries were washed in phosphate-buffered saline (PBS) solution to remove residual blood and excess connective tissue was also removed. The processed samples were then cryo-preserved at -80^{o}C. Before scanning, the samples were removed from cryo-preservation media, washed with pbs and cut into 3 cm long cylindrical portions. Two samples were cut open longitudinally to estimate the influence of residual stress on the arterial wall structure and two additional samples were cut open and fixed flat on a holding surface. Each sample was placed in 8 mm NMR tubes containing deionised (DI) water.

MR Microimaging

DTI was performed at room temperature on a horizontal bore 7T MRI scanner (Bruker, Etlingen, Germany) with shielded gradients (maximum gradient strength = 770 mT/m, rise time = 115 µs) and ^{1}H mouse cryogenic surface coil (CryoProbe, Bruker Biospin). For diffusion-weighted imaging, a 2D spin echo (SE) based DTI sequence, with a multi-shot EPI readout and unipolar diffusion sensitising pulsed field gradients placed symmetrically around the 180^{o} RF pulse, was applied using the following parameters: echo time (TE)/repetition time (TR) = 26/3500 ms; field of view (FOV) = 14.97×14.97 mm^2; matrix size = 128×128; slice thickness = 0.117 mm; voxel size = 0.117 mm^3; no inter-slice spacing; number of slices = 25; δ/Δ = 2.32/7.32 ms; b = 800 s/mm^2; with 128 directions and 10 "b = 0" reference images; number of averages = 1; no fat suppression. The total acquisition time per sample was 96 minutes. To analyse the influence of gradient strength (G) and effective diffusion time ($\tau = \Delta - \delta/3$), sample no. 5 was also scanned at a b-value of 1200 s/mm^2. This was achieved by increasing G while keeping τ the same as that of the b_{800} acquisition. The same sample was then scanned at a much higher b value of 1600 s/mm^2, keeping G constant (same as b_{800} acquisition) whilst τ was changed (δ/Δ = 3.10/8.10 ms). To calculate the apparent diffusion coefficient (ADC), two samples were scanned at 7 different b-values ranging from 0 to 1000 s/mm^2 (0, 150, 250, 400, 600, 800, 1000 s/mm^2). All the imaging parameters remained the same as outlined above, except for each b-value, diffusion sensitising gradients were applied in six noncollinear directions and the number of averages was set to 3. The acquisition time per sample, in this case, was 82 minutes. For each acquisition, the corresponding T1-weighted and T2-weighted (non-EPI) images were also acquired with the same FOV and isotropic voxel resolution of 0.117 mm^3. These anatomical scans were later used in the post-processing to compensate for susceptibility-induced off-resonance fields in diffusion-weighted images (DWIs).

Post-processing and fibre tractography

ExploreDTI (v4.8.5) was used to process each DTI dataset [25]. The post-processing steps included Gibbs ringing correction, interslice instability correction, correction for eddy current-induced distortions and correction for susceptibility artefacts [26-28]. The diffusion tensor profile was estimated on the corrected images using a robust fitting routine provided in ExploreDTI [29, 30]. Directionally invariant indices such as fractional anisotropy (FA), mean diffusivity (MD), axial diffusivity (AD), radial diffusivity (RD) and geometric measures such as C_L (linear tensor profile), C_P (planar tensor profile) and C_S (spherical tensor profile) [31] were exported from ExploreDTI in NIfTI

format for further analysis. 6D diffusion tensor datasets were also exported in NIfTI format. The diffusion tensor was then imported in DSIStudio [32] using a custom-built Matlab routine for deterministic tractography. Fibre tractography was performed for each DTI dataset using the following parameters: FA tracking threshold = [0.1 1], fibre length range = [0.5 50] mm; angle threshold = 20 degree, step size = 0.05 mm, tracking algorithm = Euler, and interpolation method = cubic. For each dataset 5000 fibre tracts were generated and exported in a text format. The exported fibre tracts were then used to calculate the helical angle, dispersion parameter (κ) and fibre curvature using custom-built Matlab routines. These routines were verified and validated using simulated fibre angle data.

Multi b-value estimation

To calculate the apparent diffusion coefficient (ADC) the two multi b-value scans were used. From each acquisition, ROIs encompassing the entire media layer were manually drawn on selected slices. Since an inversion recovery pulse was not used in the multi b-value scan, each ROI was eroded by a factor of 2 voxels (inward and outward) to avoid the partial volume effect (PVE). A nonlinear least-squares Levenberg-Marquardt algorithm was used for each pixel in the ROI to fit DW signal intensity decay *S* with diffusion-weighting *b* to a mono-exponential function of the form:

$$S = S_0 e^{\sum_{i=1}^{3}\sum_{j=1}^{3} b_{ij} ADC_{ij}} \quad (1.1)$$

where *S* is the b-dependent signal intensity of the image, S_0 is the signal intensity without the diffusion sensitization; b_{ij} is the *i*, *jth* component of the diffusion-weighting b-matrix, and ADC_{ij}, is the *i*, *jth* component of the apparent diffusion coefficient. In order to overcome the biases in ADC estimation due to the background noise, only values which exhibited at least 3 times higher amplitude than the baseline noise signal were fit to the mono-exponential curve. The noise level (S_{noise}) was defined as a standard deviation within ROIs drawn manually in peripheral airspace (background) of the image uncontaminated by artefacts. The SNR per slice in the tissue ROI was then obtained by dividing the measured signal (*S*) by the noise (S_{noise}). The averaged SNR profile of the multi-b-value data is provided in the supplementary Table 1 and the averaged SNR calculated for samples 1 – 5 is listed in supplementary Table 2. For each sample, the ADCs were assessed by independent fits for each diffusion direction and the mean ADC per voxel was obtained by averaging the six independent ADCs.

RESULTS

Quantitative assessment using directionally invariant indices

For each of the five samples scanned, using an identical acquisition protocol, a region of interest (ROI) was generated from the artefact compensated arithmetic average of 128 diffusion-encoded images (figure 1d). Scalar indices such as FA, MD, RD and AD were obtained from the calculated diffusion tensors, whilst geometric measures such as C_L, C_P, C_S, and C_A were also calculated for each sample. The median values of these indices are presented in Table 1. Figure 2 illustrates these directionally invariant indices for sample 5.

Across the media layer (inner-media to outer media), the directionally invariant indices show a radial transition in their respective values. High FA was observed in the outer media, whereas, the inner media showed comparatively lower values of FA. The response of MD was in contrast to that of FA. Similarly, C_L showed higher values in the outer media while C_S response was similar to MD. In terms of directional diffusivity, AD, was higher than RD and high RD values were mostly located close to the

fringes of the inner media (figure 2). Across the selected five samples, the minimum median value of FA was 0.20 (std 0.06) (sample 5) and the highest median value of FA was 0.32 (std 0.08) (sample2). Similarly, the minimum median value of MD was 0.79 (std 0.07) (sample 4) and the maximum median value of MD was 1.06 (std 0.10) (sample 2). Using the calculated eigenvalues, the in-plane dispersion parameter kappa (κ) was also calculated for each of the five samples. Table 1 provides the median and standard deviation values of the calculated scalar indices.

Fibre tractography-based assessment

For each dataset, 5000 fibre tracts were generated. These tracts indicate a near circumferential fibre alignment (figure 3). For sample 2 (figure 3a), the principal diffusion direction is represented (inset) in terms of an ellipsoid. These ellipsoids per voxel also indicate a near circumferential orientation of the principal fibre direction.

Scalar indices such as FA and MD were mapped onto the individual fibre tracts. These projected values are slightly different from the results of the previous section, as each fibre was generated under certain constraints. Table 2 shows these mapped values for each dataset. Figure 3 (a – e) shows the tracts of each sample and the colours on each tract represent the mapped values of helical angles. These calculated angles can be used to estimate the tract orientation and degree of alignment along any arbitrary plane. The rose plots in figure 3 (a-1 – e-1) show the circular distribution of helical angles for every dataset. The near circumferential alignment of the calculated tracts is evident from the fact that the highest median tract angle (sample4) is less than 5^{o} (Table 3), however, these fibre tracts exhibited a high degree of fibre dispersion (std ≤ 8).

In order to estimate the radial distribution of the tracts, curvature for each tract was calculated. The curvature distribution along the ellipsoidal representation (figure 3a - inset) shows that the reconstructed tracts are predominantly aligned in the circumferential direction and the degree of radial distribution is primarily less than 3 voxels (figure 4).

Effect of b-value on diffusion quantification

To analyse the sensitivity of the DW signal to various microstructural constituents in the arterial tissue, sample 5 was additionally scanned using higher b-values of 1200 (δ/Δ was kept constant and G was increased) and 1600 mm/s^2 (G was kept constant and δ/Δ were varied). Figure 5 shows an axial slice of the averaged b_{800}, b_{1200} and b_{1600} volumes and their corresponding FA and MD maps. As previously observed, these indices show a radial transition in their values (inner-media to outer media). For all three cases, high FA values were observed in the outer media, whereas the inner media showed comparatively lower FA values. The response of MD was opposite to that of FA (figure 5). In terms of directional diffusivity, AD, was in general, higher than RD (Table 4). Moreover, the increase in b-value shows changes in FA and MD across acquisitions. This behaviour was also observed for geometric measures. Table 4 shows the median values of all the calculated indices for the three b-values.

Using the aforementioned constraints, 5000 tracts were constructed for each acquisition (figure 6). For the b_{800} dataset, the mean FA along the fibre pathway was 0.22 (std 0.04), whereas, for b_{1600} the mean FA along the pathways was 0.17 (std 0.02). Table 5 provides additional statistical information on the volume occupied by the generated fibres. In terms of mean helical angle and circular distribution, acquisitions at b-values of 800 and 1200 showed comparable results (because of

identical δ/Δ), whereas, a noticeable deviation in results were observed for fibres generated at the b-value of 1600 s/mm^2. (Table 6).

Region of Interest (ROI) based analysis

To quantify local variations in arterial ultrastructure across the media layer, six ROIs were manually drawn on the selected slices of intact and open cut datasets. The ROIs M1_R/L, were traced to identify regions close to the intima-media interface, M2_R/L, were used to trace the central region of the media layer and M3_R/L, encompassed the outer region of the media layer (figure 7). Suffixes 'L' and 'R' in figure 7 represent left and right sections of each ROI, respectively. Each ROI was 2×7 mm^2. For the open cut flat samples, only three ROI were used to identify the intima-media interface, central media and outer media. Normality of distributions was tested using D'Agostino-Pearson normality test and visual inspection of variable histograms. Mean and standard deviation values of FA, MD, C_L, C_P and C_S were computed using all voxels identified by ROIs for each component (ROI) and no standardised techniques were used to normalise the indices between components. Quantitative statistical comparison of FA, MD, C_L, C_P and C_S values for each region was conducted separately for intact, open cut and open cut flat samples using unbalanced one-way analysis of variance (ANOVA). Differences were considered significant when $p < 0.05$.

For intact samples (figure 7, a – d) the geometric measures in 3P plot showed distinct clusters corresponding to each ROI. Compared to M1, a noticeable shift in pattern distribution was observed in M3. For open cut samples (figure 7, e – h), the distributions for each ROI were clustered in the same region without any clear distinction. For open cut flat samples, the 3P plots also showed a clear shift in the overall distribution, indicating a clear reorganisation of the vessel constituents (figure 7, i and j).

In terms of directionally invariant indices, intact samples showed a significant increase in anisotropy (FA) from the inner media to the outer media (figure 8, $p < 0.05$). Mean diffusivity, on the other hand, showed a significant drop in directional diffusivity in the outer media (figure 8, $p < 0.05$). Geometric measures also displayed significant differences in their mean values ($p < 0.05$). AD showed a drop across the media layer, however, the degree of drop in RD was much higher than that of the corresponding AD (not shown). For open cut samples, no significant changes were observed in FA, C_P and C_S values, whereas, MD and C_L showed significant differences, only, between M1 and M3 ROIs. For open cut flat samples, the statistical comparison did not show a significant difference in the values of FA, MD, C_L, C_P and C_S across the media layer.

Discussion and conclusion

The molecular displacement of water in a tissue can be used to provide insights into the microstructural composition of a tissue. This study shows that the constituents of the arterial tissue and their arrangement regulate water diffusion in that microenvironment. The results of this study have demonstrated the sensitivity of DTI based markers to local variations in the microenvironment of intact arterial tissues. The study has also shown the sensitivity of these biomarkers to tissue damage by quantifying structural changes associated with reduced structural integrity of the arterial tissue, namely open cut samples.

As a quantitative biomarker, the apparent diffusion coefficient (ADC) has been used in a number of in-vivo and ex-vivo studies to identify healthy and pathology-specific regions in blood vessels [33-37]. Using a mono-exponential model of diffusion-weighted signal attenuation over a range of 0 –

1000 s/mm^2, with 6 non-collinear diffusion-encoding direction, we estimated the ADC in the range of 1.37 ± 0.18 (10^{-3} mm^2/s). This estimated ADC value is comparable to the aforementioned in-vivo and ex-vivo studies [33-37]. The ADC-based assessment relies on a mono-exponential model of diffusion-weighted signal decay and is known to be a poor representation of diffusion in the complex environment of biological tissue. Directionally invariant indices such as FA and MD are much better options to estimate diffusivity, as they are derived from the diffusion tensor, which incorporates diffusion anisotropy in the mono-exponential model. In other words, the diffusion tensor reflects the underlying diffusivity profile of a biological sample irrespective of the sample orientation with respect to the scanner frame of reference [38].

Previous studies on cartilage and prostate tissues have demonstrated the efficacy of FA and MD in distinguishing between healthy and diseased tissues [39-41]. Studies on cartilage have demonstrated the sensitivity of FA to changes in collagen density in the ECM [39, 42, 43]. Furthermore, a number of experimental studies showed the dependency of MD on variation in glycosaminoglycan (GAGs) content [44-46]. Even though GAG contribution in ECM is relatively low (2 – 5 % by dry weight), recent studies have shown that GAG plays an important role in arterial homeostasis by influencing arterial viscoelasticity and residual stresses [47].

Figure 2(i) of this study shows a highly heterogeneous microenvironment in the media. The 3P plot indicates the profile of diffusion tensors as a more bloated disc-like shape. This shape distribution is indicative of the highly disperse nature of arterial fibrous structure (figure 4 – top row). These results show that the arterial tissue is considerably heterogeneous and this heterogeneity is the reason for a relatively weak diffusion anisotropy (low FA compared to the white matter of the brain). Since FA provides information on the directionality of the local diffusion profile, this parameter can be considered as a marker of arterial ultrastructure because of its sensitivity to ECM and SMC organisation and damage. Our results show FA values in the range of 0.21 ±0.06 to 0.32±0.08. These results are in a close agreement with the study by Opriessnig, et al. [48]. Other directionally invariant indices such as MD, which is a measure of GAG (isotropy), RD; which is considered to be sensitive to the degree of hindrance to molecular diffusion due to ECM and SMC, is a measure of fibre density and AD; the measure of diffusivity along the principal fibre direction, thus a possible fibre damage marker, show similar agreements [49, 50].

From histology, it can be observed that the regions close to the intima-media boundary have low elastin, collagen and SMC density and regions close to the adventitia-media interface has high elastin, collagen and SMC contents (figure 1). GAG contents, on the other hand, are much higher close to the intima-media boundary as compared to the adventitia-media region [47, 51]. To the best of our knowledge, this is the first study to provide an insight into the constituent density distribution across the media layer of an intact artery using DTI. Our results show higher structural density in the outer regions of media layer, compared to the regions close to the intima-media region. This assessment is in agreement with the work of Stergiopulos, et al. [52], where the authors reported differences in the opening angles between the inner and outer medial halves. C_L, and C_A projections in figure 2 and averaged DWI and FA projections in figure 5 of this study clearly demonstrate the feasibility of DTI in capturing the details of the ultrastructure density variations across the media of the arterial tissue.

The region of interest based analysis of this study showed that for intact samples, the directionally invariant indices and calculated geometric measures exhibited significant differences across the media layer (figure 8, a – e). FA, C_L and C_P were higher close to the adventitia-media interface and MD and C_S were higher close to the media-intima boundary, and vice-versa (figures 2 and 8). However, the planar (C_P) and the spherical (C_S) tensor profile did not show statistically significant

difference between M1 and M2 ROIs. The 3P plots also show three distinct clusters corresponding to the three selected ROIs (figure 7, a – d). All these results highlight the highly heterogeneous nature of the intact media layer. For open cut samples, only, MD and C_L showed significant differences in the extreme ROI comparison (M1 – M3) (figure 8, g – j). Moreover, the 3P plots showed an observable overlap in the clusters (figure 7, e – h). For open cut flat samples, the study did not find statistically significant differences in DTI derived markers across the media layer (figure 8, k – o) and the 3P plots showed a high degree of cluster overlap (figure 7, i and j). Since the transmural distribution of GAGs plays an important role in regulating the residual stresses in the arterial tissue [47], we speculate that the release of residual stresses by cutting a vessel and then placing it flat may have contributed to the changes in the microstructural environment of the tissue.

Directionally invariant indices such as FA and MD, and fibre tractography based assessments such as helical angle and fibre dispersion are highly sensitive to a number of acquisition and post-processing parameters. For instance, use of anisotropic voxel resolution for fibre reconstruction is known to bias the tractography reconstruction [53-55]. Similarly, larger voxel size will incorporate more PVE [56], which would suggest it is the reason for disparity among DTI and SHG or PLM based fibre assessment. To address these shortcomings of previous DTI based studies [19, 21], our assessment was carried out at 0.117 mm^3 isotropic voxel resolution.

Selection of an optimal b-value is another important aspect to consider [19, 38]. b-value is related to the gradient strength (G) and the effective diffusion time (Δ-δ/3), therefore any change in either of these will evidently change the diffusion profile (figure 5). Depending upon the structural dimensions of collagen, elastin, GAG and SMC, all these macromolecules pose hindrance to water diffusion to a varying degrees. DTI studies on articular cartilage showed that the DW signal contains information of all the tissue constituents and the calculated DTI tensor contains additional information such as the volume fraction corresponding to individual constituents, their respective local orientation and respective degree of alignment [39, 43, 46, 57]. Based on the previous work of Flamini, et al. [19], we analysed the influence of b-value on fibre tract assessment. By changing the b-value from 800 to 1200 and then to 1600 s/mm^2, we observed noticeable changes in scalar indices and fibre tract profiles. When we kept the gradient amplitude fixed and changed the b-value by changing the effective diffusion time, we observed the transition from hindered diffusion to restricted diffusion (figures 5 and 6) [38]. Since the DTI model cannot accurately map non-Gaussian diffusion effects (restricted diffusion), it is not suitable to map diffusion profile at higher b-values. This limitation of the DTI model may explain the apparent drop in the values of directionally invariant indices at high b-values. Nevertheless, this transition (hindered to restricted) highlights the contribution of various constituents in modulating the diffusion-weighted signal decay at various diffusion-encoding timings.

The results of this study are based on small ex-vivo intact common carotid artery segments. These samples were scanned in DI water without inducing any kind of mechanical loading. Therefore, care must be taken while interpreting these results for in-vivo assessment, as physiological loading might alter the results. However, a recent study by Spronck, et al. [7], has demonstrated a minimal effect of physiological loading on the circumferential orientation of VSMC in murine carotid arteries. In general, arterial tissue exhibits short T2 decay and compared to intima and media, the adventitia has the shortest T2 relaxation time [58]. In this study we did not perform T2 parametric estimation to calculate the T2 profile of the tissue. Using the available information from literature on arterial tissue characterisation, while considering the dependency of T2 on B0 field and to maintain a sufficient SNR, we selected a TE of 26 ms [58-62]. Even though, the selected TE is well within the range of the suggested values, the microenvironment in the adventitia layer exhibited poor SNR and

therefore, was not included in the assessment, however, by using stimulated echo rather than a spin echo based sequence, it is possible to further reduce TE and thus map the adventitia layer [63]. In this study, sufficient SNR was achieved by minimising the TE and as a direct consequence, the narrow pulse approximation (NPA) was violated [64]. There are a number of important issues to consider while adopting a dMRI from dNMR models and one of the considerations is "*The narrow pulse approximation (NPA) is unrealistic*" [65]. A number of studies have also shown that the violation of the NPA only leads to a modified interpretation from the Ensemble average propagator (EAP) towards a "center-of-mass propagator", which represents the mean of the spin positions (trajectories) during the first gradient and the second gradient pulse [66]. As a result, diffusion displacements are slightly underestimated and EAP blurs out, however, the characteristics of the global spin propagator remains unchanged [67]. In addition, contrary to general understanding, there are a number of studies which suggest that a long delta (δ) might be more suitable in terms of estimating the orientation and density of fibrous structures [68-70].

In conclusion, this study has demonstrated the applicability of DTI framework, based on optimised multi-segmented EPI-DWI acquisition protocol, as a reliable, fast and non-invasive method to quantify the ultrastructure of intact arterial tissue. The study has demonstrated the sensitivity of DTI based biomarkers to structural variations across the media layer of arterial tissue and has also shown the influence of residual stresses in maintaining the structural heterogeneity of arterial tissue. Thus the presented pipeline can be used to acquire a deeper understanding of structural remodelling under pathological conditions such as atherosclerosis and aneurysm.

References:

[1] J. A. Rhodin, "Architecture of the vessel wall," *Comprehensive Physiology,* 2011.

[2] M. P. Jacob, "Extracellular matrix remodeling and matrix metalloproteinases in the vascular wall during aging and in pathological conditions," *Biomedicine & Pharmacotherapy,* vol. 57, no. 5, pp. 195-202, 2003.

[3] M. P. Jacob, C. Badier-Commander, V. Fontaine, Y. Benazzoug, L. Feldman, and J. B. Michel, "Extracellular matrix remodeling in the vascular wall," *Pathol Biol (Paris),* vol. 49, no. 4, pp. 326-32, May 2001.

[4] Mohamed A. Gaballa, Christopher T. Jacob, Yhomas E. Rayn, Jin Liu, Bruce Simon, and S. Goldman, "Large Artery Remodeling During Aging: Biaxial passive and active stiffness," *Hypertension,* vol. 32, pp. 437-443, 1998.

[5] H. C. Stary *et al.*, "A definition of the intima of human arteries and of its atherosclerosis-prone regions. A report from the Committee on Vascular Lesions of the Council on Arteriosclerosis, American Heart Association," *Circulation,* vol. 85, no. 1, p. 391, 1992.

[6] F. W. Keeley and A. Alatawi, "Response of Aortic Elastin Synthesis and Accumulation to Developing Hypertension and the Inhibitory Effect of Colchicine on This Response," (in English), *Laboratory Investigation,* vol. 64, no. 4, pp. 499-507, Apr 1991.

[7] B. Spronck, R. T. Megens, K. D. Reesink, and T. Delhaas, "A method for three-dimensional quantification of vascular smooth muscle orientation: application in viable murine carotid arteries," *Biomechanics and modeling in mechanobiology,* vol. 15, no. 2, pp. 419-432, 2016.

[8] I. Hariton, G. de Botton, T. C. Gasser, and G. A. Holzapfel, "Stress-driven collagen fiber remodeling in arterial walls," *Biomech Model Mechanobiol,* vol. 6, no. 3, pp. 163-75, Apr 2007.

[9] C. Pagiatakis, R. Galaz, J. C. Tardif, and R. Mongrain, "A comparison between the principal stress direction and collagen fiber orientation in coronary atherosclerotic plaque fibrous caps," (in English), *Medical & Biological Engineering & Computing,* vol. 53, no. 6, pp. 545-555, Jun 2015.

[10] M. J. Kääb, K. Ito, B. Rahn, J. M. Clark, and H. P. Nötzli, "Effect of mechanical load on articular cartilage collagen structure: a scanning electron-microscopic study," *Cells Tissues Organs,* vol. 167, no. 2-3, pp. 106-120, 2000.

[11] M. K. O'Connell *et al.*, "The three-dimensional micro-and nanostructure of the aortic medial lamellar unit measured using 3D confocal and electron microscopy imaging," *Matrix Biology,* vol. 27, no. 3, pp. 171-181, 2008.

[12] S. K. de Visser *et al.*, "Anisotropy of collagen fibre alignment in bovine cartilage: comparison of polarised light microscopy and spatially resolved diffusion-tensor measurements," *Osteoarthritis and Cartilage,* vol. 16, no. 6, pp. 689-697, 2008.

[13] B. Wicker, H. Hutchens, Q. Wu, A. Yeh, and J. Humphrey, "Normal basilar artery structure and biaxial mechanical behaviour," *Computer methods in biomechanics and biomedical engineering,* vol. 11, no. 5, pp. 539-551, 2008.

[14] P. B. Dobrin, "Effect of histologic preparation on the cross-sectional area of arterial rings," *Journal of Surgical Research,* vol. 61, no. 2, pp. 413-415, 1996.

[15] N. Ugryumova, S. V. Gangnus, and S. J. Matcher, "Three-dimensional optic axis determination using variable-incidence-angle polarization-optical coherence tomography," *Optics letters,* vol. 31, no. 15, pp. 2305-2307, 2006.

[16] N. Ugryumova, D. P. Attenburrow, C. P. Winlove, and S. J. Matcher, "The collagen structure of equine articular cartilage, characterized using polarization-sensitive optical coherence tomography," *Journal of Physics D: Applied Physics,* vol. 38, no. 15, p. 2612, 2005.

[17] Y. Xia, J. B. Moody, and H. Alhadlaq, "Orientational dependence of T2 relaxation in articular cartilage: A microscopic MRI (μMRI) study," *Magnetic resonance in medicine,* vol. 48, no. 3, pp. 460-469, 2002.

[18] V. Flamini, C. Kerskens, C. Simms, and C. Lally, "Fibre orientation of fresh and frozen porcine aorta determined non-invasively using diffusion tensor imaging," *Medical engineering & physics,* vol. 35, no. 6, pp. 765-776, 2013.

[19] V. Flamini, C. Kerskens, K. M. Moerman, C. K. Simms, and C. Lally, "Imaging Arterial Fibres Using Diffusion Tensor Imaging—Feasibility Study and Preliminary Results," *EURASIP Journal on Advances in Signal Processing,* vol. 2010, no. 1, pp. 1-13, 2010.

[20] S. Ghazanfari, A. Driessen-Mol, G. J. Strijkers, F. P. Baaijens, and C. V. Bouten, "The evolution of collagen fiber orientation in engineered cardiovascular tissues visualized by diffusion tensor imaging," *PloS one,* vol. 10, no. 5, p. e0127847, 2015.

[21] S. Ghazanfari, A. Driessen-Mol, G. J. Strijkers, F. M. Kanters, F. P. Baaijens, and C. V. Bouten, "A comparative analysis of the collagen architecture in the carotid artery: second harmonic generation versus diffusion tensor imaging," *Biochem Biophys Res Commun,* vol. 426, no. 1, pp. 54-8, Sep 14 2012.

[22] D. K. Jones, *Diffusion mri*. Oxford University Press, 2010.

[23] D. K. Jones and M. Cercignani, "Twenty-five pitfalls in the analysis of diffusion MRI data," *NMR Biomed,* vol. 23, no. 7, pp. 803-20, Aug 2010.

[24] S. Brockstedt, J. R. Moore, C. Thomsen, S. Holtas, and F. Stahlberg, "High-resolution diffusion imaging using phase-corrected segmented echo-planar imaging," (in English), *Magnetic Resonance Imaging,* vol. 18, no. 6, pp. 649-657, Jul 2000.

[25] A. Leemans, B. Jeurissen, J. Sijbers, and D. Jones, "ExploreDTI: a graphical toolbox for processing, analyzing, and visualizing diffusion MR data," in *17th Annual Meeting of Intl Soc Mag Reson Med*, 2009, vol. 209, p. 3537.

[26] A. Leemans and D. K. Jones, "The B-Matrix Must Be Rotated When Correcting for Subject Motion in DTI Data," (in English), *Magnetic Resonance in Medicine,* vol. 61, no. 6, pp. 1336-1349, Jun 2009.

[27] M. O. Irfanoglu, L. Walker, J. Sarlls, S. Marenco, and C. Pierpaoli, "Effects of image distortions originating from susceptibility variations and concomitant fields on diffusion MRI tractography results," *Neuroimage,* vol. 61, no. 1, pp. 275-88, May 15 2012.

[28] J. D. Tournier, S. Mori, and A. Leemans, "Diffusion tensor imaging and beyond," *Magn Reson Med,* vol. 65, no. 6, pp. 1532-56, Jun 2011.

[29] J. Veraart, J. Sijbers, S. Sunaert, A. Leemans, and B. Jeurissen, "Weighted linear least squares estimation of diffusion MRI parameters: strengths, limitations, and pitfalls," *Neuroimage,* vol. 81, pp. 335-46, Nov 01 2013.

[30] C. M. Tax, W. M. Otte, M. A. Viergever, R. M. Dijkhuizen, and A. Leemans, "REKINDLE: robust extraction of kurtosis INDices with linear estimation," *Magn Reson Med,* vol. 73, no. 2, pp. 794-808, Feb 2015.

[31] C. F. Westin, S. Peled, H. Gudbjartsson, R. Kikinis, and F. A. Jolesz, "Geometrical diffusion measures for MRI from tensor basis analysis," in *Proceedings of ISMRM*, 1997, vol. 97, p. 1742.

[32] F. C. Yeh, T. D. Verstynen, Y. Wang, J. C. Fernandez-Miranda, and W. Y. Tseng, "Deterministic diffusion fiber tracking improved by quantitative anisotropy," *PLoS One,* vol. 8, no. 11, p. e80713, 2013.

[33] V. E. Young *et al.*, "Diffusion-weighted magnetic resonance imaging for the detection of lipid-rich necrotic core in carotid atheroma in vivo," *Neuroradiology,* vol. 52, no. 10, pp. 929-36, Oct 2010.

[34] Y. B. Xie *et al.*, "High resolution 3D diffusion cardiovascular magnetic resonance of carotid vessel wall to detect lipid core without contrast media," (in English), *Journal of Cardiovascular Magnetic Resonance,* vol. 16, no. 1, p. 1, Sep 17 2014.

[35] Y. Qiao, I. Ronen, J. Viereck, F. L. Ruberg, and J. A. Hamilton, "Identification of atherosclerotic lipid deposits by diffusion-weighted imaging," *Arterioscler Thromb Vasc Biol,* vol. 27, no. 6, pp. 1440-6, Jun 2007.

[36] S. E. Kim *et al.*, "In vivo and ex vivo measurements of the mean ADC values of lipid necrotic core and hemorrhage obtained from diffusion weighted imaging in human atherosclerotic plaques," *Journal of Magnetic Resonance Imaging,* vol. 34, no. 5, pp. 1167-1175, 2011.

[37] J. F. Toussaint, J. F. Southern, V. Fuster, and H. L. Kantor, "Water diffusion properties of human atherosclerosis and thrombosis measured by pulse field gradient nuclear magnetic resonance," *Arterioscler Thromb Vasc Biol,* vol. 17, no. 3, pp. 542-6, Mar 1997.

[38] P. Tofts, *Quantitative MRI of the brain: measuring changes caused by disease*. John Wiley & Sons, 2005.

[39] X. Deng, M. Farley, M. T. Nieminen, M. Gray, and D. Burstein, "Diffusion tensor imaging of native and degenerated human articular cartilage," *Magn Reson Imaging,* vol. 25, no. 2, pp. 168-71, Feb 2007.

[40] R. Bourne, N. Kurniawan, G. Cowin, P. Sved, and G. Watson, "16 T diffusion microimaging of fixed prostate tissue: preliminary findings," *Magn Reson Med,* vol. 66, no. 1, pp. 244-7, Jul 2011.

[41] R. M. Bourne, N. Kurniawan, G. Cowin, P. Sved, and G. Watson, "Microscopic diffusion anisotropy in formalin fixed prostate tissue: preliminary findings," *Magn Reson Med,* vol. 68, no. 6, pp. 1943-8, Dec 2012.

[42] J. G. Raya *et al.*, "Change of diffusion tensor imaging parameters in articular cartilage with progressive proteoglycan extraction," *Invest Radiol,* vol. 46, no. 6, pp. 401-9, Jun 2011.

[43] R. Meder, S. K. de Visser, J. C. Bowden, T. Bostrom, and J. M. Pope, "Diffusion tensor imaging of articular cartilage as a measure of tissue microstructure," (in English), *Osteoarthritis and Cartilage,* vol. 14, no. 9, pp. 875-881, Sep 2006.

[44] D. Burstein, M. L. Gray, A. L. Hartman, R. Gipe, and B. D. Foy, "Diffusion of Small Solutes in Cartilage as Measured by Nuclear-Magnetic-Resonance (Nmr) Spectroscopy and Imaging," (in English), *Journal of Orthopaedic Research,* vol. 11, no. 4, pp. 465-478, Jul 1993.

[45] Y. Xia, T. Farquhar, N. Burton-Wurster, M. Vernier-Singer, G. Lust, and L. Jelinski, "Self-diffusion monitors degraded cartilage," *Archives of biochemistry and biophysics,* vol. 323, no. 2, pp. 323-328, 1995.

[46] R. Knauss, J. Schiller, G. Fleischer, J. Karger, and K. Arnold, "Self-diffusion of water in cartilage and cartilage components as studied by pulsed field gradient NMR," (in English), *Magnetic Resonance in Medicine,* vol. 41, no. 2, pp. 285-292, Feb 1999.

[47] E. U. Azeloglu, M. B. Albro, V. A. Thimmappa, G. A. Ateshian, and K. D. Costa, "Heterogeneous transmural proteoglycan distribution provides a mechanism for regulating residual stresses in the aorta," *Am J Physiol Heart Circ Physiol,* vol. 294, no. 3, pp. H1197-205, Mar 2008.

[48] P. Opriessnig, H. Mangge, R. Stollberger, H. Deutschmann, and G. Reishofer, "In vivo cardiovascular magnetic resonance of 2D vessel wall diffusion anisotropy in carotid arteries," *J Cardiovasc Magn Reson,* vol. 18, no. 1, p. 81, Nov 23 2016.

[49] A. L. Alexander *et al.*, "Characterization of cerebral white matter properties using quantitative magnetic resonance imaging stains," *Brain connectivity,* vol. 1, no. 6, pp. 423-446, 2011.

[50] H. M. Feldman, J. D. Yeatman, E. S. Lee, L. H. Barde, and S. Gaman-Bean, "Diffusion tensor imaging: a review for pediatric researchers and clinicians," *J Dev Behav Pediatr,* vol. 31, no. 4, pp. 346-56, May 2010.

[51] J. M. Mattson, R. Turcotte, and Y. Zhang, "Glycosaminoglycans contribute to extracellular matrix fiber recruitment and arterial wall mechanics," *Biomech Model Mechanobiol,* pp. 1-13, Aug 04 2016.

[52] N. Stergiopulos, S. Vulliemoz, A. Rachev, J. J. Meister, and S. E. Greenwald, "Assessing the homogeneity of the elastic properties and composition of the pig aortic media," *J Vasc Res,* vol. 38, no. 3, pp. 237-46, May-Jun 2001.

[53] S. Vos, M. Viergever, and A. Leemans, "The anisotropic bias of fractional anisotropy in anisotropically acquired DTI data," in *Proceedings of the 19th Annual Meeting of International Society for Magnetic Resonance in Medicine, Montreal, Canada*, 2011, p. 1945.

[54] H. Oouchi *et al.*, "Diffusion anisotropy measurement of brain white matter is affected by voxel size: Underestimation occurs in areas with crossing fibers," (in English), *American Journal of Neuroradiology,* vol. 28, no. 6, pp. 1102-1106, Jun-Jul 2007.

[55] D. K. Jones, T. R. Knosche, and R. Turner, "White matter integrity, fiber count, and other fallacies: the do's and don'ts of diffusion MRI," *Neuroimage,* vol. 73, pp. 239-54, Jun 2013.

[56] L. E. Salminen, T. E. Conturo, J. D. Bolzenius, R. P. Cabeen, E. Akbudak, and R. H. Paul, "Reducing Csf Partial Volume Effects to Enhance Diffusion Tensor Imaging Metrics of Brain Microstructure," *Technol Innov,* vol. 18, no. 1, pp. 5-20, Apr 2016.

[57] J. G. Raya *et al.*, "Ultra-high field diffusion tensor imaging of articular cartilage correlated with histology and scanning electron microscopy," *MAGMA,* vol. 24, no. 4, pp. 247-58, Aug 2011.

[58] Y. Qiao, D. A. Steinman, M. Etesami, A. Martinez-Marquese, E. G. Lakatta, and B. A. Wasserman, "Impact of T2 decay on carotid artery wall thickness measurements," *Journal of Magnetic Resonance Imaging,* vol. 37, no. 6, pp. 1493-1498, 2013.

[59] Y. Qiao, I. Ronen, J. Viereck, F. L. Ruberg, and J. A. Hamilton, "Identification of atherosclerotic lipid deposits by diffusion-weighted imaging," *Arteriosclerosis, thrombosis, and vascular biology,* vol. 27, no. 6, pp. 1440-1446, 2007.

[60] J. E. Schneider *et al.*, "High-resolution, multicontrast three-dimensional-MRI characterizes atherosclerotic plaque composition in ApoE–/–mice ex vivo," *Journal of Magnetic Resonance Imaging,* vol. 20, no. 6, pp. 981-989, 2004.

[61] J.-F. Toussaint, J. F. Southern, V. Fuster, and H. L. Kantor, "T2-weighted contrast for NMR characterization of human atherosclerosis," *Arteriosclerosis, thrombosis, and vascular biology,* vol. 15, no. 10, pp. 1533-1542, 1995.

[62] J.-F. Toussaint, J. F. Southern, V. Fuster, and H. L. Kantor, "Water diffusion properties of human atherosclerosis and thrombosis measured by pulse field gradient nuclear magnetic resonance," *Arteriosclerosis, Thrombosis, and Vascular Biology,* vol. 17, no. 3, pp. 542-546, 1997.

[63] J. E. Tanner, "Use of the stimulated echo in NMR diffusion studies," *The Journal of Chemical Physics,* vol. 52, no. 5, pp. 2523-2526, 1970.

[64] P. T. Callaghan, *Principles of nuclear magnetic resonance microscopy*. Oxford University Press on Demand, 1993.

[65] A. Özcan, K. H. Wong, L. Larson-Prior, Z. H. Cho, and S. K. Mun, "Background and mathematical analysis of diffusion mri methods," *International journal of imaging systems and technology,* vol. 22, no. 1, pp. 44-52, 2012.

[66] P. P. Mitra and B. I. Halperin, "Effects of Finite Gradient-Pulse Widths in Pulsed-Field-Gradient Diffusion Measurements," (in English), *Journal of Magnetic Resonance Series A,* vol. 113, no. 1, pp. 94-101, Mar 1995.

[67] V. J. Wedeen, P. Hagmann, W. Y. Tseng, T. G. Reese, and R. M. Weisskoff, "Mapping complex tissue architecture with diffusion spectrum magnetic resonance imaging," *Magn Reson Med,* vol. 54, no. 6, pp. 1377-86, Dec 2005.

[68] M. Hall and D. Alexander, "Finite pulse widths improve fibre orientation estimates in diffusion tensor MRI," in *Proc. Intl. Soc. Mag. Reson. Med*, 2006, vol. 14, p. 1076.

[69] D. Raffelt *et al.*, "Apparent fibre density: a novel measure for the analysis of diffusion-weighted magnetic resonance images," *Neuroimage,* vol. 59, no. 4, pp. 3976-3994, 2012.

[70] C.-H. Yeh, J.-D. Tournier, K.-H. Cho, C.-P. Lin, F. Calamante, and A. Connelly, "The effect of finite diffusion gradient pulse duration on fibre orientation estimation in diffusion MRI," *Neuroimage,* vol. 51, no. 2, pp. 743-751, 2010.

[71] D. Le Bihan, C. Poupon, A. Amadon, and F. Lethimonnier, "Artifacts and pitfalls in diffusion MRI," *J Magn Reson Imaging,* vol. 24, no. 3, pp. 478-88, Sep 2006.

LIST OF FIGURES

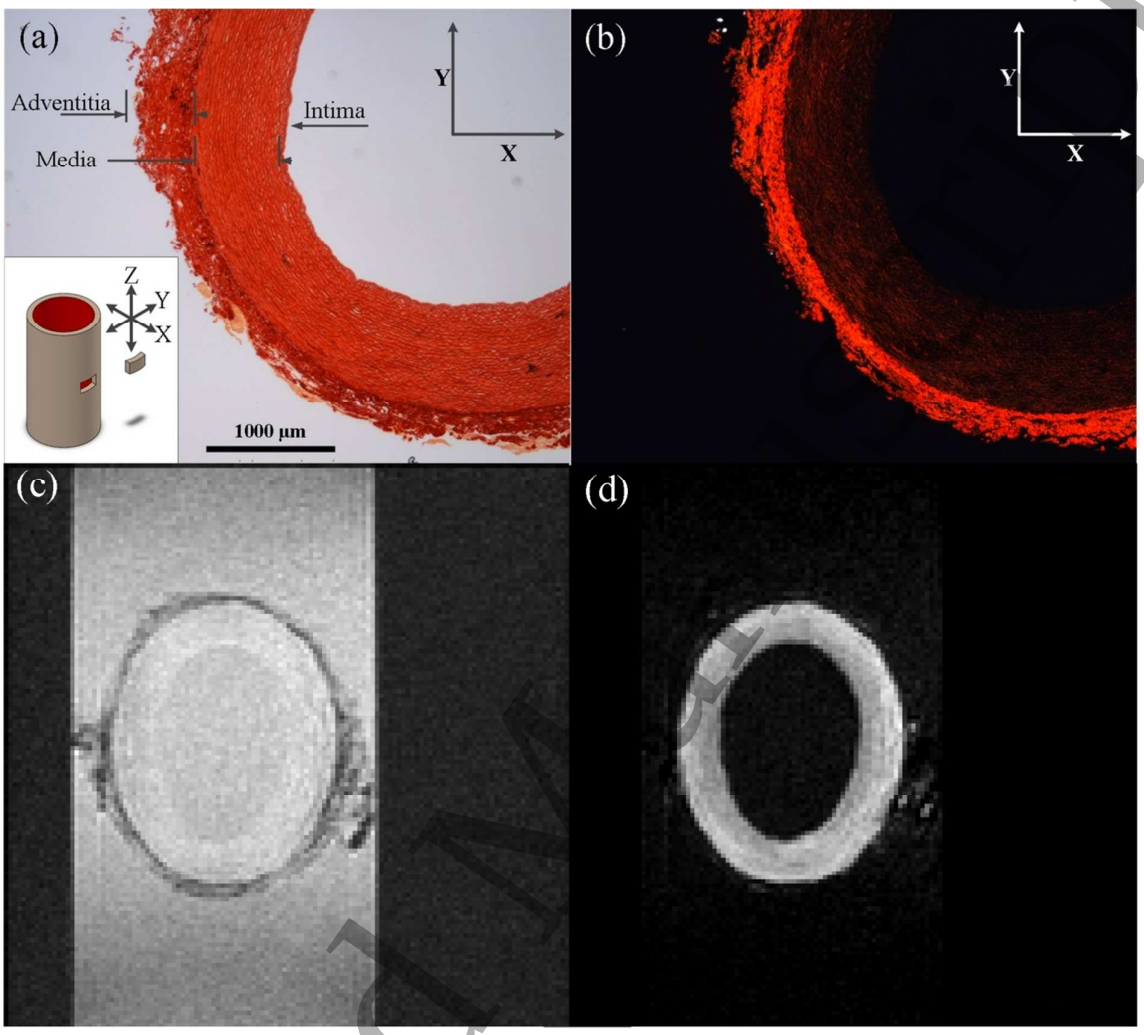

Figure 1: (a) Histological ring section of a porcine common carotid artery stained with picrosirius red under light microscopy. (b) Same stained image under polarised light to isolate collagen fibres from the rest of the constituents (magnification 2X). (c) Dorsal view of an axially acquired T2-weighted image of a common carotid artery. (d) Diffusion-weighted image of the same slice. This image is an arithmetic mean of 128 diffusion-encoded images. MRI images were acquired with an isotropic voxel resolution of 0.117mm^3 and a b-value of 800 s/mm^2. (Histological image and MRI images are from different samples and are representative images).

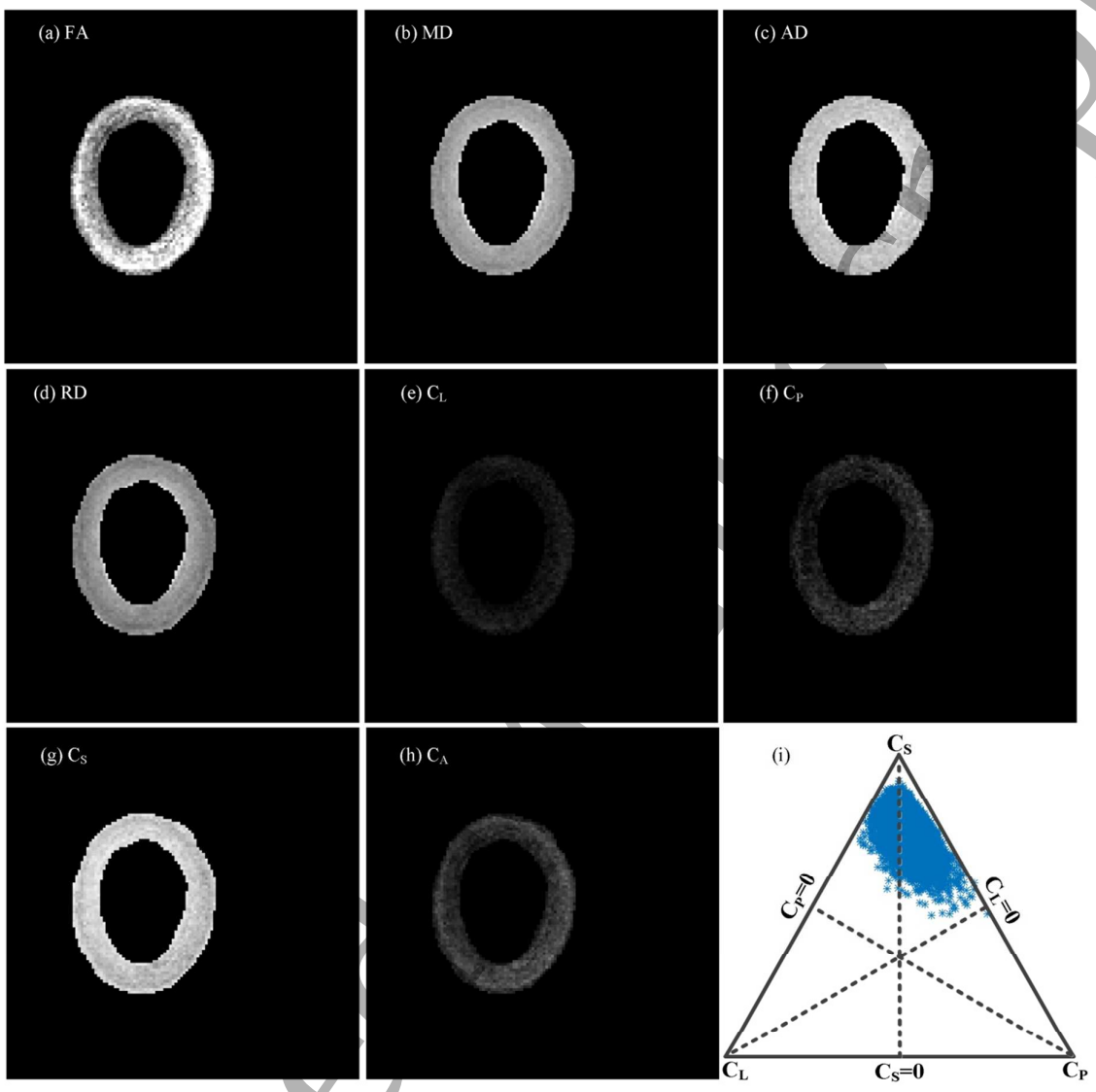

Figure 2: Directionally invariant indices and geometric measures (a – h) to highlight regions of anisotropic and isotropic diffusion in the ROI. (i) Isotropic/anisotropic diffusion representation using barycentric space. The estimated C_L and C_P values for the tensor measurements of the media are shown. The 3 Phase plot shows that the diffusion in the ROI has mainly planar anisotropy.

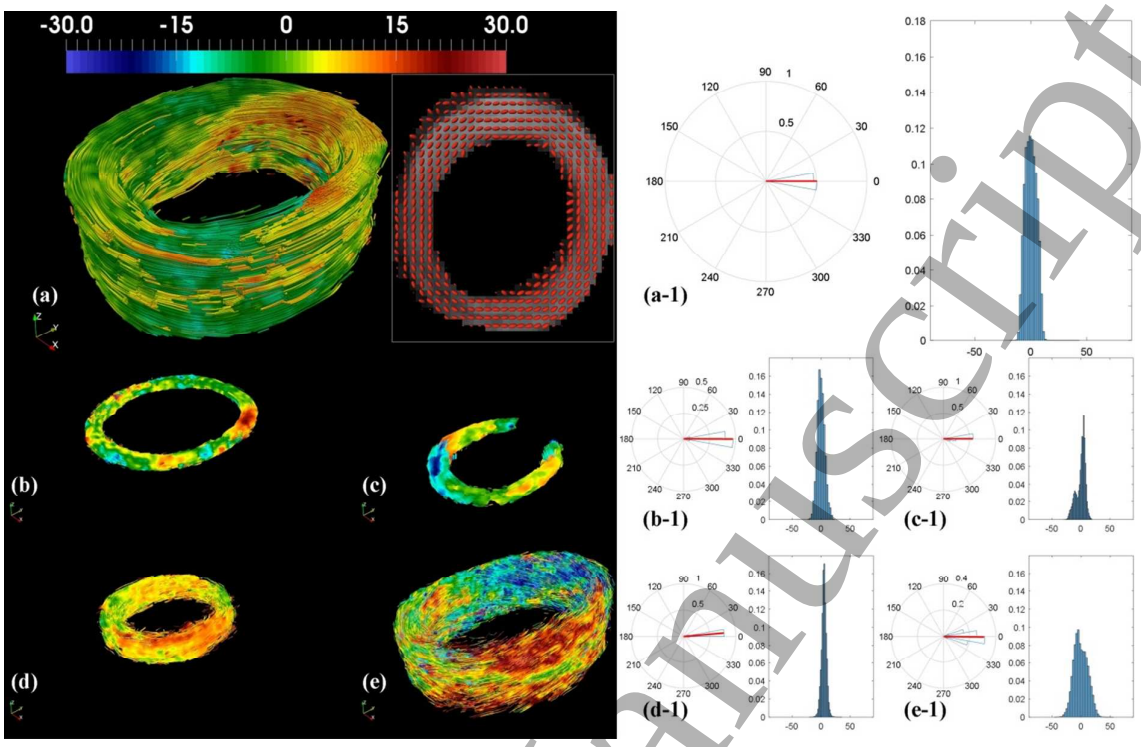

Figure 3: Projection of helical angles on calculated fibre tracts (a – e). Inset in (a) shows the ellipsoidal representation of the main fibre orientation in an axial plane of sample 2. a-1 to e-1, The circular and linear distribution of the helical angles along with their respective median values. a and a-1, represent the helical angle projections and distribution, respectively, of sample 2. b and b-1, The same indices for sample 1. c – e and c-1 – e -1, represent the indices for sample 3, 4 and 5 respectively.

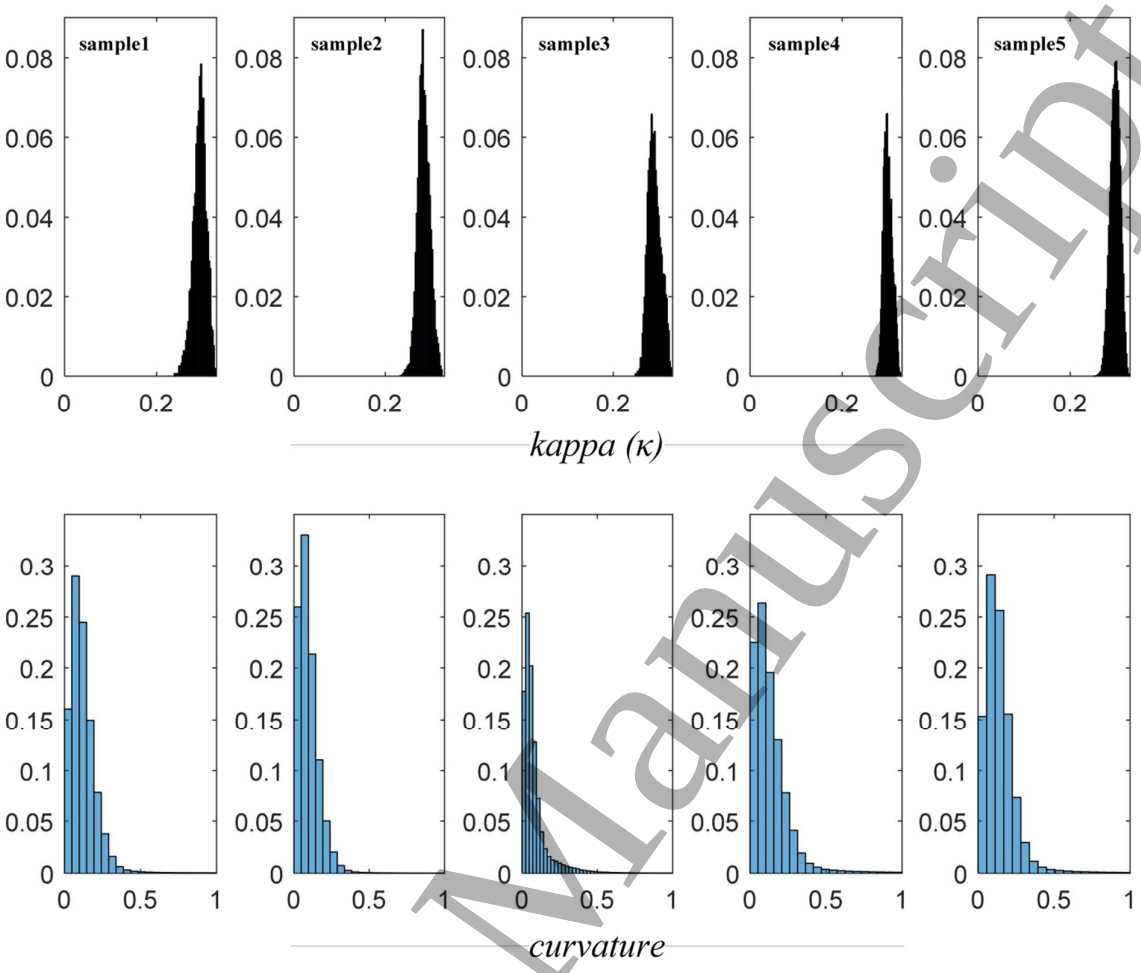

Figure 4: First row, histogram density plots of dispersion parameter kappa (κ; 0 – anisotropic 1/3 – isotropic) for each of the selected five samples. Second row, distribution plots of fibre curvature, highlighting the radial dispersion in calculated fibre tracts. Mostly the curvature values are less than 0.3 mm, indicating that the fibres usually do not cross radially.

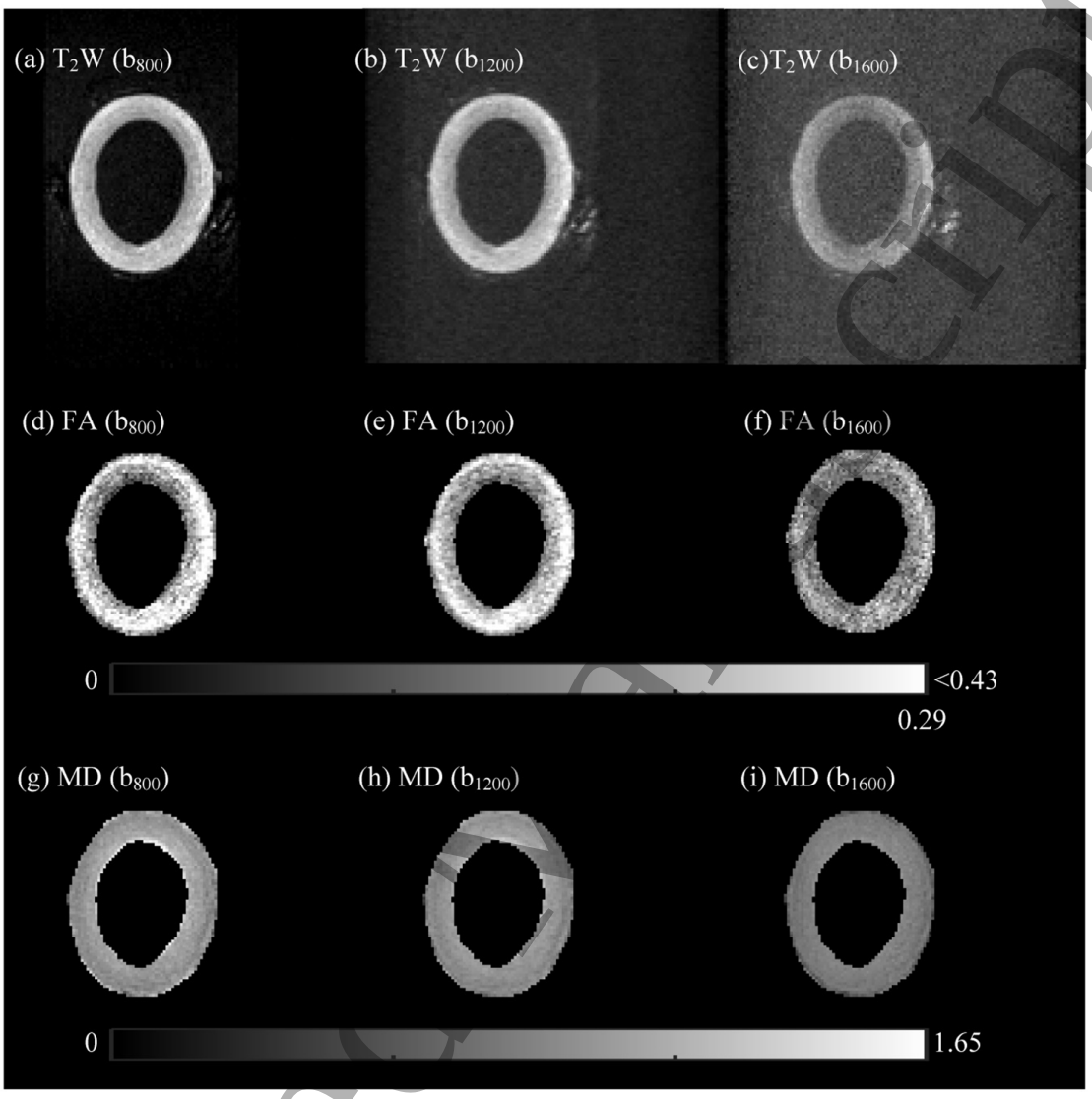

Figure 5: Effect of b-value on diffusion parameters. (a – c), Diffusion-weighted images (arithmetic average of 128 diffusion-encoded directions). Regions of low diffusivity have bright contrast, whereas, regions of high diffusivity are represented by darker shades of grey. Because of the possible 'T2 shine through' effect, these artefact-compensated averaged DWIs were not included in the quantitative assessment [71]. (d –f), Variation in FA profile due to change in b-value. (g –h), Mean diffusivity (MD $\times 10^{-3}$) under different b-values. The maximum FA was obtained from b_{800} scan.

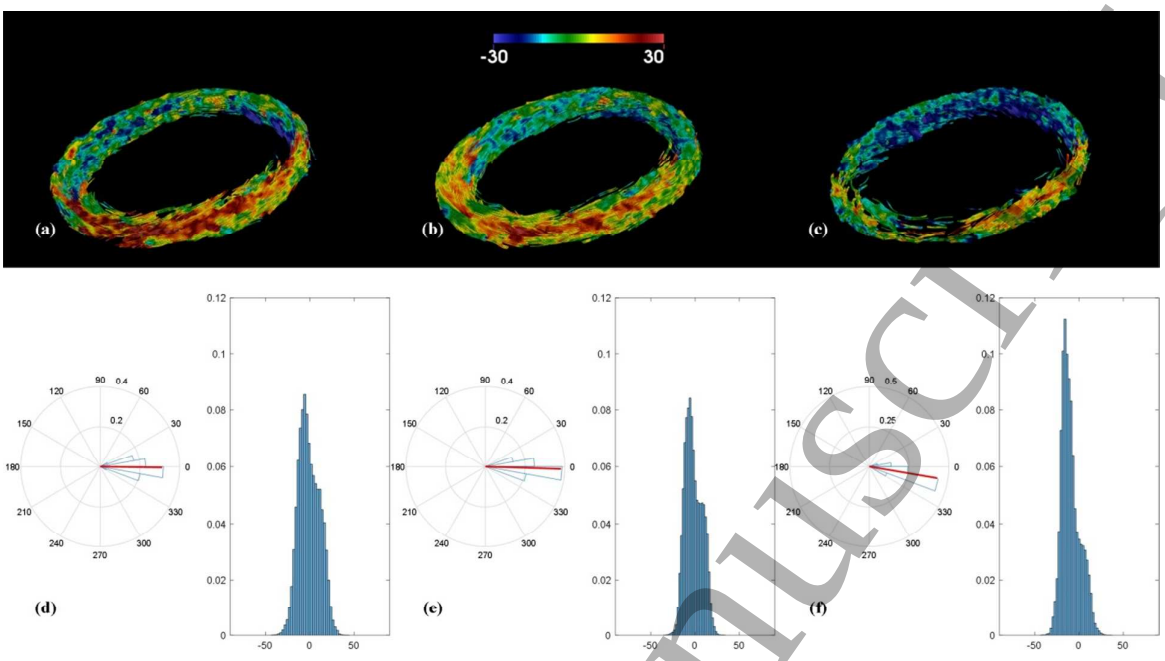

Figure 6: (a – c) Projection of calculated helical angles on individual fibre tracts. The tracts were generated from the same sample using the same ROI and same constraints. Each scan was obtained using identical acquisition protocol. The only difference across the scans was in the b-value. (a) The effective b-value was 800 s/mm^2. (b) The effective b-value was 1200 s/mm^2. This b-value was achieved by increasing the gradient strength (G). (c) The effective b-value was 1600 s/mm^2. For this scan, the gradient strength was kept the same as that of in 'a' and the effective diffusion time was increased to achieve high b-value. (d - f), Circular and linear distributions of the calculated helical angles.

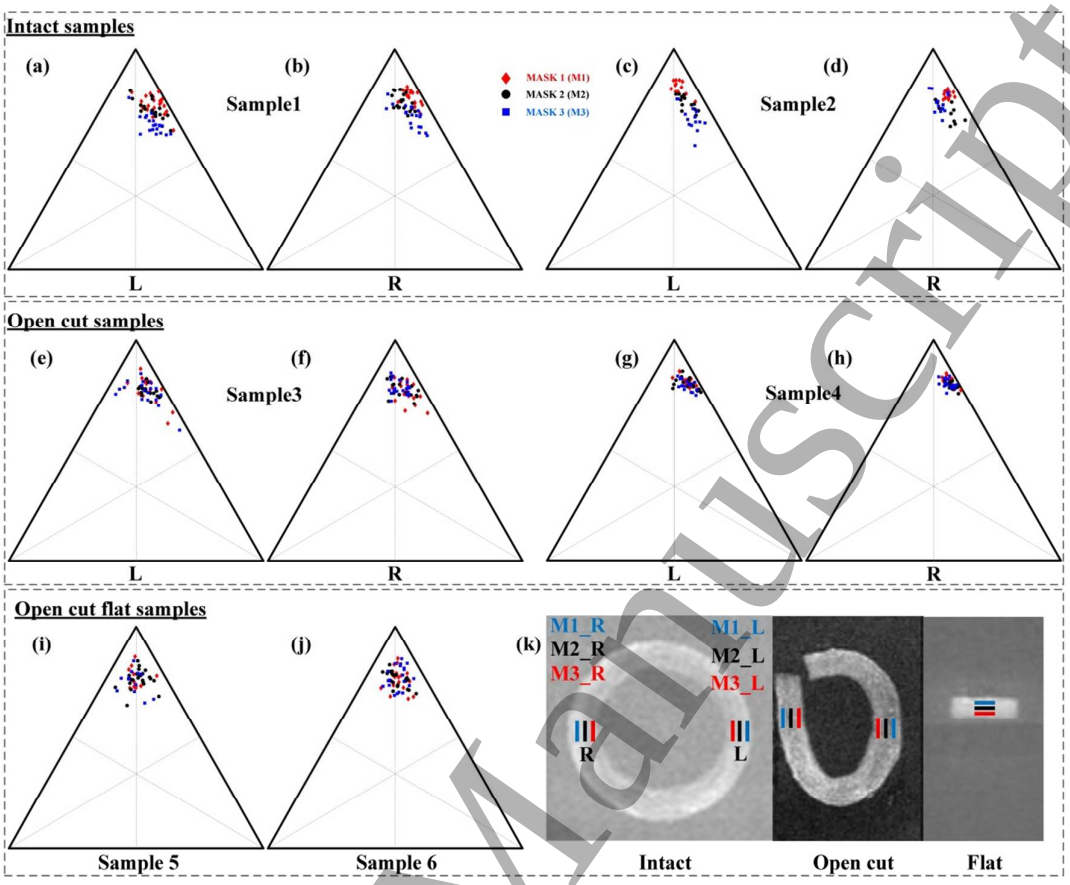

Figure 7: Isotropic/anisotropic diffusion representation using barycentric space (3P). The estimated C_L and C_P values for the tensor measurements for three regions of media are shown. (a and b), 3P plot for intact sample 1, (c and d), C_L, C_P and C_S distribution for intact sample 2. (e and f) and (g and h), Estimated geometric measures in each ROI for open cut samples and (i and j), The distribution of two open cut flat samples. (k), Each ROI and their respective location in intact, open cut and open cut flat samples.

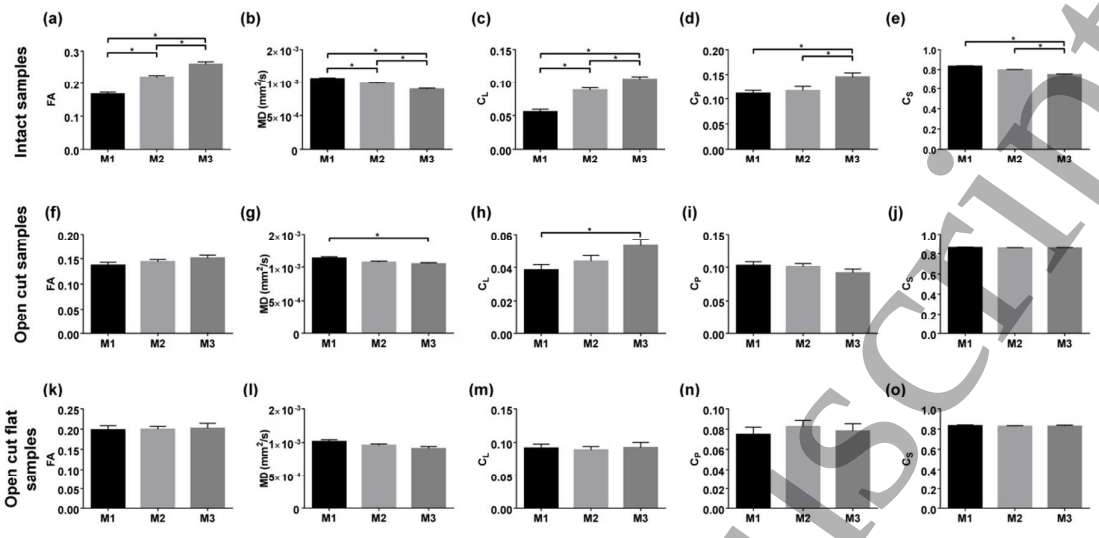

Figure 8: Quantification of arterial tissue heterogeneity. Directionally invariant indices and geometric measures are displayed as columns (means) for each ROI. (a – e), Intact samples (n = 16, two ROIs per slice, 4 slices per assessment and two samples), (f – j), Open cut samples (n = 16, two ROIs per slice, 4 slices per assessment and two samples). (k – o), Open cut flat samples (n = 8, one ROI per slice, 4 slices per assessment and two samples). Values represent mean ± SEM. *p < 0.05.

LIST OF TABLES

Table 1: Median and the standard deviation of directionally invariant indices and geometric measures for the selected five samples

Scalar indices (median)	Sample1	Sample2	Sample3	Sample4	Sample5
FA (std)	0.23(0.08)	0.32(0.08)	0.30(0.08)	0.27(0.07)	0.20(0.06)
MD (std)	0.89(0.11)	1.06(0.10)	0.95(0.09)	0.79(0.07)	1.05(0.11)
AD (std)	1.10(0.11)	1.38(0.10)	1.20(0.12)	0.96(0.08)	1.27(0.11)
RD (std)	0.78(0.12)	0.90(0.12)	0.82(0.09)	0.71(0.07)	0.94(0.12)
C_L (std)	0.08(0.03)	0.07(0.03)	0.06(0.03)	0.03(0.01)	0.07(0.03)
C_P (std)	0.15(0.08)	0.28(0.09)	0.28(0.09)	0.28(0.08)	0.12(0.05)
C_S (std)	0.76(0.09)	0.63(0.10)	0.64(0.10)	0.68(0.08)	0.80(0.06)
κ (std)	0.29(0.01)	0.28(0.01)	0.29(0.01)	0.29(0.01)	0.29(0.01)

Table 2: Median and the standard deviation of directionally invariant indices along the reconstructed fibre tracts

Scalar indices (median)	Sample1	Sample2	Sample3	Sample4	Sample5
FA (std)	0.26(0.06)	0.33(0.07)	0.34(0.05)	0.29(0.04)	0.22(0.04)
MD (std)	0.81(0.14)	1.01(0.19)	0.91(0.10)	0.75(0.08)	0.96(0.13)
AD (std)	1.02(0.17)	1.37(0.18)	1.17(0.16)	0.93(0.10)	1.19(0.15)
RD (std)	0.71(0.13)	0.87(0.14)	0.77(0.10)	0.66(0.07)	0.85(0.12)

Table 3: Median and standard deviation of calculated helical angles

Sample no.	Median helical angle (deg)	Std
1	-0.62	6.30
2	-0.22	4.58
3	2.04	7.44
4	4.92	4.01
5	1.58	5.46

Table 4: Median and the standard deviation of scalar indices and geometric measures under different b-values

Scalar indices (median)	b800	b1200	b1600
FA (std)	0.20 (0.06)	0.20 (0.05)	0.15 (0.04)
MD (std)	1.05 (0.11)	0.98 (0.11)	0.83 (0.09)
AD (std)	1.27 (0.11)	1.19 (0.12)	0.95 (0.10)
RD (std)	0.94 (0.15)	0.89 (0.12)	0.77 (0.09)
C_L (std)	0.07 (0.03)	0.05 (0.03)	0.04 (0.02)
C_P (std)	0.12 (0.05)	0.15 (0.05)	0.12 (0.04)
C_S (std)	0.80 (0.06)	0.78 (0.06)	0.84 (0.04)

Table 5: Median and the standard deviation of directionally invariant indices along the reconstructed fibre tracts. For each acquisition (dataset), 5000 fibre tracts were generated.

Scalar indices (median)	b800	b1200	b1600
FA (std)	0.22 (0.04)	0.23 (0.04)	0.17 (0.02)
MD (std)	0.96 (0.13)	0.92 (0.13)	0.77 (0.09)
AD (std)	1.19 (0.15)	1.12 (0.15)	0.90 (0.10)
RD (std)	0.85 (0.12)	0.81 (0.12)	0.71 (0.08)

Table 6: Median and standard deviation of calculated helical angles

Sample b-value	median helical angle (deg)	std
800	1.58	5.46
1200	3.15	9.64
1600	11.51	10.42